PHYSICAL REVIEW LETTERS **120**, 107703 (2018)

Editors' Suggestion

Tunable $\Gamma - K$ Valley Populations in Hole-Doped Trilayer WSe_2

Hema C. P. Movva,[1] Timothy Lovorn,[2] Babak Fallahazad,[1] Stefano Larentis,[1] Kyounghwan Kim,[1]
Takashi Taniguchi,[3] Kenji Watanabe,[3] Sanjay K. Banerjee,[1] Allan H. MacDonald,[2] and Emanuel Tutuc[1,*]
[1] *Microelectronics Research Center, Department of Electrical and Computer Engineering,*
The University of Texas at Austin, Austin, Texas 78758, USA
[2] *Department of Physics, The University of Texas at Austin, Austin, Texas 78712, USA*
[3] *National Institute of Materials Science, 1-1 Namiki Tsukuba, Ibaraki 305-0044, Japan*

(Received 1 November 2017; revised manuscript received 7 January 2018; published 9 March 2018)

We present a combined experimental and theoretical study of valley populations in the valence bands of trilayer WSe_2. Shubnikov–de Haas oscillations show that trilayer holes populate two distinct subbands associated with the K and Γ valleys, with effective masses $0.5m_e$ and $1.2m_e$, respectively; m_e is the bare electron mass. At a fixed total hole density, an applied transverse electric field transfers holes from Γ orbitals to K orbitals. We are able to explain this behavior in terms of the larger layer polarizability of the K orbital subband.

DOI: 10.1103/PhysRevLett.120.107703

Transition metal dichalcogenides (TMDs) are layered materials that possess strong spin-orbit coupling, have large carrier effective masses, and can be isolated down to a monolayer, making them attractive hosts for phenomena associated with strong spin-orbit and electron-electron interactions. Symmetry considerations dictate that monolayer $2H$-TMDs possess band extrema at the time-reversed partner K and K' Brillouin zone corners with a finite gap between dipole coupled conduction and valence bands [1]. Beyond the monolayer limit, the TMD band structure becomes more complicated. Specifically, the locations of the band extrema in few-layer TMDs [2,3], and their dependence on externally controllable parameters like transverse gate electric (E) fields, have, for most TMDs [4–7], remained open questions that can be answered only by combining experiment and theory.

Here, we address the band maxima and impact of an E field in the valence band of trilayer WSe_2, a TMD with large valence band spin-orbit splitting [8], high mobility, and robust low temperature Ohmic contacts [9–11]. Recent studies have shown that the valence band maxima are located at the K points in mono- and bilayer WSe_2, and at the Γ point in bulk WSe_2 [3,12]. Using magnetotransport measurements, we show that in high mobility WSe_2 trilayers encapsulated in h-BN, holes populate two distinct subbands with different effective masses, $0.5m_e$ and $1.2m_e$, that we associate with the K and Γ valleys, respectively; m_e is the bare electron mass. At a fixed total hole density, the K and Γ occupations can be tuned by an applied E field in a dual-gated device, with Γ being the lowest-energy state at low E field and K being the lowest-energy state at high E field. *Ab initio* calculations support these findings and explain the shift of the valence band maxima, and the consequent transfer of holes from Γ to K with an increasing E value.

Our samples consist of WSe_2 trilayers exfoliated from bulk crystals (HQ Graphene). Figure 1(a) shows the room temperature photoluminescence (PL) spectrum of trilayer $2H$-WSe_2, which has distinct peaks corresponding to the indirect (1.45 eV) and direct (1.60 eV) energy gap transitions [13]. The PL spectrum combined with optical contrast and Raman spectroscopy enables an unambiguous identification of trilayer WSe_2. The Fig. 1(a) inset shows the optical micrograph of an h-BN encapsulated, dual-gated trilayer WSe_2 Hall bar sample, fabricated using a van der Waals assembly technique [9,14]. Ohmic hole contacts down to cryogenic temperatures were achieved using bottom Pt electrodes in combination with a large, negative top-gate bias (V_{TG}) [9,10]. The dual-gated device structure allows independent control of the WSe_2 hole carrier density

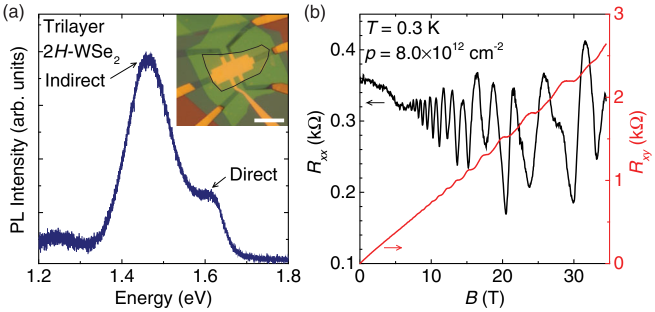

FIG. 1. (a) Room temperature PL spectrum of trilayer $2H$-WSe_2 acquired with 532 nm wavelength excitation. The peaks corresponding to the direct and indirect gap transitions are labeled. (Inset) Optical micrograph of a dual-gated trilayer WSe_2 Hall bar. The black line marks the contour of the WSe_2 flake. The scale bar is 10 μm. (b) Trilayer WSe_2 R_{xx} and R_{xy} vs B measured at $T = 0.3$ K and $p = 8.0 \times 10^{12}$ cm^{-2}.

0031-9007/18/120(10)/107703(5)

(p) and the E field. Magnetotransport measurements were conducted using low-frequency lock-in techniques at temperatures down to $T = 0.3$ K, and perpendicular magnetic fields up to $B = 35$ T. Three samples were investigated in this Letter, all with consistent results. Here, we focus on data from two samples. Figure 1(b) shows the longitudinal (R_{xx}) and Hall (R_{xy}) resistance vs B for a trilayer $\mathrm{WSe_2}$ sample at $V_{\mathrm{TG}} = -8.5$ V, and a back-gate bias, $V_{\mathrm{BG}} = 0$ V. The hole density is $p = 8.0 \times 10^{12}$ $\mathrm{cm^{-2}}$, as extracted from the slope of R_{xy} at low B fields. The R_{xx} data show well-defined Shubnikov–de Haas (SdH) oscillations accompanied by the emergence of quantum Hall state plateaux in R_{xy} coincident with R_{xx} minima at high B fields. Unlike holes in mono- and bilayer $\mathrm{WSe_2}$ at $V_{\mathrm{BG}} = 0$ V, which show one fundamental SdH oscillation frequency, corresponding to a single populated subband [10], the trilayer data of Fig. 1(b) show a clear beating pattern, suggestive of holes populating multiple subbands.

To investigate the origin of the SdH oscillations beating pattern, we performed magnetotransport measurements as a function of V_{TG} and V_{BG}. Figure 2(a) shows R_{xx} vs B measured in a second trilayer $\mathrm{WSe_2}$ sample with a top- (back-) gate capacitance, $C_{\mathrm{TG}} = 120$ $\mathrm{nF/cm^2}$ ($C_{\mathrm{BG}} = 130$ $\mathrm{nF/cm^2}$), at different V_{TG} values, $V_{\mathrm{BG}} = 0$ V, and $T = 1.5$ K. Figure 2(b) shows the Fourier transform (FT) amplitude of the R_{xx} vs B^{-1} data of Fig. 2(a), which shows two principal peaks that differ markedly in their response to V_{TG}. While the low-frequency peak increases in frequency with $|V_{\mathrm{TG}}|$, the high-frequency peak position is nearly independent of V_{TG}. A similar set of R_{xx} vs B data at different V_{BG} values, and a fixed V_{TG} value is discussed in the Supplemental Material [15]. The presence of two principal SdH frequency peaks in the FT data suggests the existence of holes at the Fermi level in two distinct subbands. The dependence of the two FT peaks on V_{TG} in Fig. 2(b) suggests that the two subbands have very different spatial confinement properties.

To probe the nature of the subbands further, we measured the SdH oscillations T dependence. Figure 2(c) shows R_{xx} vs B at $V_{\mathrm{TG}} = -12$ V, $V_{\mathrm{BG}} = 0$ V, at various T values, and Fig. 2(d) the corresponding FT data. The FT amplitudes of the two peaks show distinct T dependence, with the high-frequency peak decaying more rapidly with T compared to the low-frequency peak. This observation is indicative of different effective masses for holes in the two subbands. We extracted the individual effective mass (m^*) associated with each subband as follows. First, we isolated the FT peak of interest by applying a bandpass filter centered at its peak and performed an inverse FT. We then performed a Dingle factor fit to each peak's inverse FT oscillation amplitude (ΔR_{xx}) vs T data at a fixed B field, $\Delta R_{xx} \propto \xi / \sinh \xi$, where $\xi = 2\pi^2 k_B T / \hbar \omega_c$ and $\omega_c = eB/m^*$ [Fig. 2(d) inset]; $\hbar$ is the reduced Planck's constant, and k_B is the Boltzmann constant. Figure 2(e) summarizes the extracted m^* vs B at two densities. At $V_{\mathrm{TG}} = -12$ V, $V_{\mathrm{BG}} = 0$ V, corresponding to $p = 8.0 \times 10^{12}$ $\mathrm{cm^{-2}}$, holes associated with the low- (high-) frequency subband have $m^* = 0.5 m_e$ ($m^* = 1.2 m_e$). The lower m^* value matches closely with $m^* = 0.45 m_e$ measured for K valley holes in mono- and bilayer $\mathrm{WSe_2}$ [10], while the larger m^* value is closer to $m^* = 0.89 m_e$ measured for Γ valley holes in few-layer $\mathrm{WSe_2}$ [27]. We therefore assign the light (heavy) holes to the K (Γ) valley of trilayer $\mathrm{WSe_2}$. At $V_{\mathrm{TG}} = -12$ V, $V_{\mathrm{BG}} = 6$ V ($p = 3.0 \times 10^{12}$ $\mathrm{cm^{-2}}$), only $m^* = 0.5 m_e$ FT peaks are observed, implying that only the K valley is populated [15].

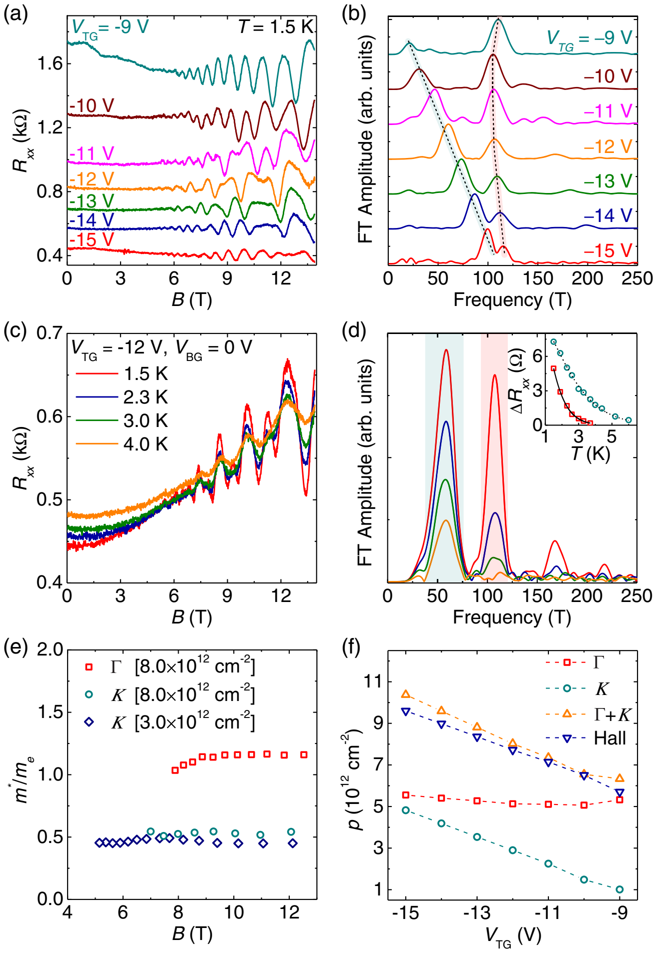

FIG. 2. (a) R_{xx} vs B at various V_{TG} values, $V_{\mathrm{BG}} = 0$ V, and $T = 1.5$ K. (b) FT amplitude of the R_{xx} vs B^{-1} data of (a). The traces are shifted for clarity in (a) and (b). The solid (dashed) line tracks the high- (low-) frequency peak in (b). (c) R_{xx} vs B measured at $V_{\mathrm{TG}} = -12$ V, $V_{\mathrm{BG}} = 0$ V, and at different T values. (d) FT amplitude of the R_{xx} vs B^{-1} data of (c). (Inset) ΔR_{xx} vs T at $B = 8.5$ T calculated from the inverse FT of the (d) data, using bandpass filters (shaded bands). The dashed (solid) line shows the Dingle factor fit to the low- (high-) frequency peak. (e) m^*/m_e vs B at $V_{\mathrm{TG}} = -12$ V, $V_{\mathrm{BG}} = 0$ V ($p = 8.0 \times 10^{12}$ $\mathrm{cm^{-2}}$), and at $V_{\mathrm{TG}} = -12$ V, $V_{\mathrm{BG}} = 6$ V ($p = 3.0 \times 10^{12}$ $\mathrm{cm^{-2}}$). The light (heavy) holes belong to the K (Γ) valley. (f) p vs V_{TG} associated with the individual FT peaks of (b) data, their sum, and Hall measurements.

To substantiate this interpretation, we compare the Hall densities with the densities associated with the FT peak

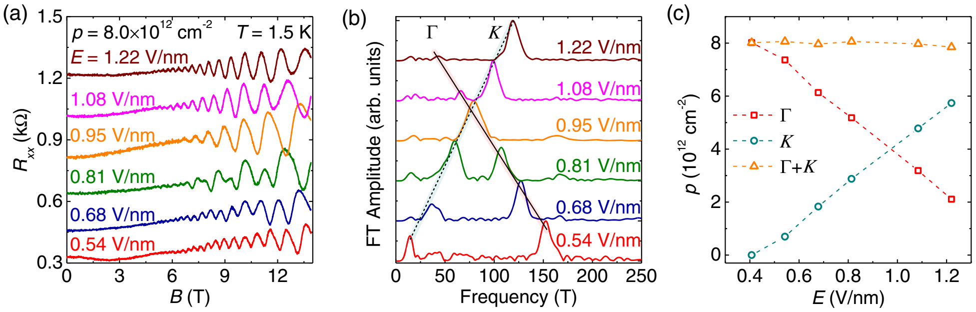

FIG. 3. (a) R_{xx} vs B at various E values, $p = 8.0 \times 10^{12}$ cm^{-2}, and $T = 1.5$ K. (b) FT amplitude of the R_{xx} vs B^{-1} data of (a). The traces are shifted for clarity in (a) and (b). The Γ (K) peak frequency decreases (increases) with increasing E values. The solid and dashed lines are guides for the eye. (c) p vs E associated with the Γ and K valleys show a linear decrease (increase) of the Γ (K) valley density with increasing E values. The sum $(\Gamma + K)$ is $p = 8 \times 10^{12}$ cm^{-2}. The two peaks overlap at $E = 0.95$ V/nm.

frequency (f), $p = g \times e/h \times f$, where g is the Landau level (LL) degeneracy of the subband associated with f, e is the electron charge, and h is Planck's constant. Figure 2(f) shows p vs V_{TG} determined from Hall measurements, along with the individual K and Γ valley densities, and their sum $(\Gamma + K)$ determined from the two FT peaks of Fig. 2(b) data using $g = 2$. The close match between the Hall and $\Gamma + K$ densities validates our valley designation. The $g = 2$ LL degeneracy for holes in both Γ and K valleys in WSe$_2$ is consistent with previous magnetotransport studies [10,27].

To assess the impact of the transverse E field on the Γ and K valley densities, we performed magnetotransport measurements as a function of $E = |C_{\mathrm{TG}}V_{\mathrm{TG}} - C_{\mathrm{BG}}V_{\mathrm{BG}}|/2\epsilon_0$, and at constant total density; ϵ_0 is the vacuum permittivity. Figure 3(a) shows R_{xx} vs B at a series of E values, for a constant $p = 8.0 \times 10^{12}$ cm^{-2}, and $T = 1.5$ K. The R_{xx} SdH oscillations beating pattern changes with the E field, suggesting an E dependence of the relative valley occupations. Figure 3(b) shows the FT data associated with Fig. 3(a); the Γ (K) peak frequency and the corresponding density decreases (increases) with increasing E values. Figure 3(c) summarizes the individual Γ, K valley densities vs E extracted from the FT peaks of Fig. 3(b). At low E fields, a majority of the holes reside in the Γ valley and progressively get transferred to the K valley with increasing E values. This observation demonstrates that the $\Gamma - K$ splitting in the valence band of trilayer WSe$_2$ is E-field dependent.

To understand the origin of the E-field-dependent $\Gamma - K$ splitting, we performed fully relativistic density functional theory (DFT) calculations for the trilayer 2H-WSe$_2$ system [15] under the local-density approximation [28], using the QUANTUM ESPRESSO distribution [29]. As shown in Fig. 4(a), we find that the valence band maximum at the K point responds much more strongly to the E field than the valence band maximum at Γ. A small E field is sufficient to induce substantial localization of the three high energy K subbands in the individual WSe$_2$ layers, leading to a threefold splitting of these states, which increases nearly linearly with E, shown in Fig. 4(b). Tracking the difference between the valence band maxima $E_\Gamma - E_K$, shown by the red squares in Fig. 4(c), we find that the highest-energy valence band shifts from Γ to K for $E \gtrapprox 0.9$ V/nm.

From the DFT calculation at each E value, we extract a tight-binding model for the valence and conduction bands near the Fermi level using WANNIER90 [30]. From each tight-binding model, we then construct $\mathbf{k}\cdot\mathbf{p}$ models for

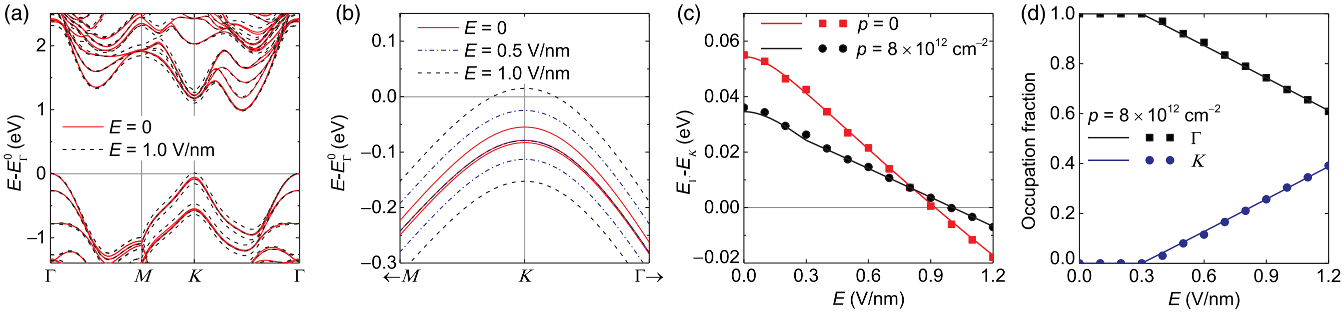

FIG. 4. (a) Band structure of trilayer 2H-WSe$_2$ with and without an E field. Energies are given relative to the valence band maximum at Γ at $E = 0$. (b) Enlarged view of the valence band maximum at K, showing an approximately linear shift with the E field. (c) E-field dependence of $E_\Gamma - E_K$, at zero and a finite hole density. (d) E-field dependence of the relative occupation of the Γ and K valleys at a fixed $p = 8 \times 10^{12}$ cm^{-2}. In (c) and (d), the symbols (lines) show results where the E field is included via the DFT calculation (the $\mathbf{k}\cdot\mathbf{p}$ model).

states in the K and Γ valleys, defined on a basis of two states in each WSe_2 layer, capturing the six highest valence bands. The E dependence of the layer "on-site" energies yields an effective dielectric constant, $\epsilon_{r,v}^* = 2eEd/(E_{v,\mathrm{top}} - E_{v,\mathrm{bot}})$; d is the displacement of each WSe_2 layer—i.e., the transverse distance between the W atoms—and $E_{v,\mathrm{top}}$ and $E_{v,\mathrm{bot}}$ are the on-site energies for states in the top and bottom layers in the valley $v = K$ or Γ. Averaging the values obtained at K and Γ for E values from 0.5 to 1.2 V/nm, we find an effective dielectric constant, $\epsilon_r^* = 7.87$, comparable to the value of 7.2 previously observed in multilayer WSe_2 [31]. Using our value of ϵ_r^*, we can generate a $\mathbf{k}\cdot\mathbf{p}$ model for any E value from the $\mathbf{k}\cdot\mathbf{p}$ model at $E = 0$ by adding eEd/ϵ_r^* to the on-site energies for the top layer and $-eEd/\epsilon_r^*$ to the on-site energies for the bottom layer. The evolution with E of the difference in valence band maxima $E_\Gamma - E_K$ for $\mathbf{k}\cdot\mathbf{p}$ models obtained in this way is shown in Fig. 4(c).

The origin of the different E-field dependences at K and Γ is the difference in orbital character of the corresponding eigenstates. Specifically, the valence band maximum states at K have opposite angular momenta and hence opposite spin in outside and interior layers, which suppresses the hybridization between adjacent layers. At $E = 0$, the highest- and lowest-energy states among the top group of three valence states at K are dominated by amplitudes on the top and bottom layers combined with even and odd parity, respectively. These subbands have dominant d-orbital amplitudes with $|l_z = -2, \downarrow\rangle$ representations on the top and bottom layers, and a much smaller $|l_z = +2, \downarrow\rangle$ amplitude on the middle layer. Importantly, because of the change in the sign of l_z, the on-site energy on the middle layer is shifted to lower energy by the spin-orbit interaction, explaining its small amplitude in the high energy subbands. The middle state among the three high energy subbands is dominated by a middle layer d-orbital amplitude with the same l_z character as its outer layer cousins, but opposite spin. Like the outside layer subbands, it is localized in the middle layer by spin-orbit splitting of the $\uparrow$ d-orbital on-site energies. As E is increased, the spin-orbit split character of the states at K is retained, leading to strong localization of subband wave functions on individual layers for $E \gtrsim 0.1$ V/nm. At Γ, on the other hand, the eigenstate amplitudes include similar $l_z = 0$ representations on all layers, allowing for large effective interlayer coupling and explaining a greatly reduced rate of change of the eigenstates and their energies with increasing E values.

To compare the theoretical results with the experimental data of Fig. 3(c), we consider the equilibrium distribution at a finite hole density. We calculate the Fermi energy for a given total hole density using an effective-mass parametrization of the highest valence bands. Holes are distributed among layers and valleys accounting for screening self-consistently with a simple electrostatic model, considering a planar charge distribution at each W layer. The variation of $E_\Gamma - E_K$ with E is modified in the presence of holes, as shown in Fig. 4(c). The distribution of holes between the Γ and K valleys as a function of E is shown in Fig. 4(d), displaying a trend which is qualitatively consistent with the measured occupations of Fig. 3(c). We obtain a hole effective mass at Γ (K) of $m_\Gamma^* = 0.82m_e$ ($m_K^* = 0.35m_e$). These m^* values are smaller than the measured masses, but they have a similar ratio. Considering the mass difference, the transfer of holes from Γ to K in our model is expected to begin at a smaller E field and to proceed more slowly with increasing E values, both features seen by comparing the Figs. 3(c) and 4(d) data. The ~50% reduction of the calculated hole transfer rate compared to the experiments is larger than the ~30% reduction that would be expected due to the smaller calculated effective masses, and the corresponding reduction in density of states. The remaining difference may be attributable to the neglect of interaction effects beyond the Hartree level, and the simplicity of the screening model. Specifically, exchange interactions are expected to further increase the E_K value as these orbitals become occupied, and to enhance the rate of change of $E_\Gamma - E_K$ with the E field.

Figure 2(b) data can be explained as follows. At low $|V_{\mathrm{TG}}|$, a majority of the holes reside in the Γ valley, thanks to a large $E_\Gamma - E_K$ value at low E fields. Increasing $|V_{\mathrm{TG}}|$ increases the E field and the total density while decreasing $E_\Gamma - E_K$. The concomitant density increase and the $E_\Gamma - E_K$ decrease result in a nearly constant Γ valley density.

In summary, we observe and explain the exceptional sensitivity of $\Gamma - K$ valley hole populations in trilayer WSe_2 to applied transverse electric fields. Given the distinct properties of holes in the two valleys characterized by differences in effective mass, spatial localization, and Berry curvature [32], the E field can be used as an effective knob to tune the electronic and spin transport properties in trilayer WSe_2, thereby making it an interesting system for valleytronics [1,32]. As an example, trilayer WSe_2 is a unique system for tuning the spin Hall effect [33] by transferring carriers from the Γ to the K valley using a transverse electric field.

This work was supported by the Nanoelectronics Research Initiative SWAN center and Intel Corporation. T. L. and A. H. M. acknowledge support from the Department of Energy, Office of Basic Energy Sciences under Contract No. DE-FG03-02ER45958, and from the Welch Foundation under Grant No. TBF1473. The authors acknowledge the Texas Advanced Computing Center (TACC) at The University of Texas at Austin for providing HPC resources that have contributed to the research results reported in this Letter. A portion of this work was performed at the National High Magnetic Field Laboratory, which is supported by National Science Foundation Cooperative Agreement No. DMR-1157490 and the State of Florida.

H. C. P. M. and T. L. contributed equally to this work.

---

[*] etutuc@mer.utexas.edu

[1] D. Xiao, G.-B. Liu, W. Feng, X. Xu, and W. Yao, Phys. Rev. Lett. **108**, 196802 (2012).

[2] P.-C. Yeh *et al.*, Phys. Rev. B **91**, 041407(R) (2015).

[3] Y. Zhang *et al.*, Nano Lett. **16**, 2485 (2016).

[4] A. Ramasubramaniam, D. Naveh, and E. Towe, Phys. Rev. B **84**, 205325 (2011).

[5] H. Yuan *et al.*, Nat. Phys. **9**, 563 (2013).

[6] T. Chu, H. Ilatikhameneh, G. Klimeck, R. Rahman, and Z. Chen, Nano Lett. **15**, 8000 (2015).

[7] J. Klein, J. Wierzbowski, A. Regler, J. Becker, F. Heimbach, K. Müller, M. Kaniber, and J. J. Finley, Nano Lett. **16**, 1554 (2016).

[8] Z. Y. Zhu, Y. C. Cheng, and U. Schwingenschlögl, Phys. Rev. B **84**, 153402 (2011).

[9] H. C. P. Movva, A. Rai, S. Kang, K. Kim, B. Fallahazad, T. Taniguchi, K. Watanabe, E. Tutuc, and S. K. Banerjee, ACS Nano **9**, 10402 (2015).

[10] B. Fallahazad, H. C. P. Movva, K. Kim, S. Larentis, T. Taniguchi, K. Watanabe, S. K. Banerjee, and E. Tutuc, Phys. Rev. Lett. **116**, 086601 (2016).

[11] S. Xu *et al.*, 2D Mater. **3**, 021007 (2016).

[12] C. Zhang, Y. Chen, A. Johnson, M.-Y. Li, L.-J. Li, P. C. Mende, R. M. Feenstra, and C.-K. Shih, Nano Lett. **15**, 6494 (2015).

[13] W. Zhao, Z. Ghorannevis, L. Chu, M. Toh, C. Kloc, P.-H. Tan, and G. Eda, ACS Nano **7**, 791 (2013).

[14] K. Kim *et al.*, Nano Lett. **16**, 1989 (2016); L. Wang *et al.*, Science **342**, 614 (2013).

[15] See Supplemental Material at http://link.aps.org/supplemental/10.1103/PhysRevLett.120.107703, which includes Refs. [16–26], for the SdH oscillation V_{BG} dependence, and for details of the *ab initio* and $\mathbf{k} \cdot \mathbf{p}$ calculations.

[16] T. Gould, S. Lebègue, and J. F. Dobson, J. Phys. Condens. Matter **25**, 445010 (2013).

[17] C. R. C. Rêgo, L. N. Oliveira, P. Tereshchuk, and J. L. F. D. Silva, J. Phys. Condens. Matter **27**, 415502 (2015).

[18] M. Schlipf and F. Gygi, Comput. Phys. Commun. **196**, 36 (2015).

[19] D. R. Hamann, Phys. Rev. B **88**, 085117 (2013).

[20] F. A. Rasmussen and K. S. Thygesen, J. Phys. Chem. C **119**, 13169 (2015).

[21] J. P. Perdew, K. Burke, and M. Ernzerhof, Phys. Rev. Lett. **77**, 3865 (1996).

[22] W. S. Yun, S. W. Han, S. C. Hong, I. G. Kim, and J. D. Lee, Phys. Rev. B **85**, 033305 (2012).

[23] L. Bengtsson, Phys. Rev. B **59**, 12301 (1999).

[24] S. Fang, R. Kuate Defo, S. N. Shirodkar, S. Lieu, G. A. Tritsaris, and E. Kaxiras, Phys. Rev. B **92**, 205108 (2015).

[25] P. Löwdin, J. Chem. Phys. **19**, 1396 (1951).

[26] T. Brumme, M. Calandra, and F. Mauri, Phys. Rev. B **91**, 155436 (2015).

[27] S. Xu *et al.*, Phys. Rev. Lett. **118**, 067702 (2017).

[28] J. P. Perdew and A. Zunger, Phys. Rev. B **23**, 5048 (1981).

[29] P. Giannozzi *et al.*, J. Phys. Condens. Matter **21**, 395502 (2009).

[30] A. A. Mostofi, J. R. Yates, G. Pizzi, Y.-S. Lee, I. Souza, D. Vanderbilt, and N. Marzari, Comput. Phys. Commun. **185**, 2309 (2014).

[31] K. Kim, S. Larentis, B. Fallahazad, K. Lee, J. Xue, D. C. Dillen, C. M. Corbet, and E. Tutuc, ACS Nano **9**, 4527 (2015).

[32] D. Xiao, W. Yao, and Q. Niu, Phys. Rev. Lett. **99**, 236809 (2007).

[33] K. F. Mak, K. L. McGill, J. Park, and P. L. McEuen, Science **344**, 1489 (2014); J. Lee, K. F. Mak, and J. Shan, Nat. Nanotechnol. **11**, 421 (2016).